3

Electric and Electromagnetic Signals Under, On, and Above the Ground Surface at the Arrival of Seismic Waves

Akihiro Takeuchi[1], Kan Okubo[2] and Nobunao Takeuchi[3]
[1]*Earthquake Prediction Research Center, Institute of Oceanic Research and Development, Tokai University 3-20-1 Orido, Shimizu-ku, Shizuoka 424-8610,*
[2]*Division of Information and Communications Systems Engineering, Tokyo Metropolitan University 6-6 Asahigaoka, Hino 191-0065,*
[3]*Research Center for Predictions of Earthquakes and Volcanic Eruptions, Graduate School of Sciences, Tohoku University 6-6 Aza-aoba, Aramaki, Aoba-ku, Sendai 980-8578, Japan*

1. Introduction

Numerous reports describe electromagnetic phenomena that occur before major earthquakes: anomalous electrotelluric potential changes (Varotsos, 2005), anomalous geomagnetic fields (Fraser-Smith et al., 1990), anomalous transmission of electromagnetic waves (Hayakawa et al., 2010), electron content perturbations in the ionosphere (Oyama et al., 2008), and infrared thermal anomaly on the ground surface detected from space (Saradjian and Akhoondzadeh, 2011). Researchers, expecting that these electromagnetic phenomena are useful for short-term prediction of earthquakes, have developed observation networks of various types throughout the world (Eftaxias et al., 2004; Uyeda et al., 2009). Although many researchers have explored such seismo-electromagnetic precursors, most reports are based on retrospective analyses. Scientific proof of the precursors apparently remains elusive. Earthquake prediction using these phenomena cannot be realized easily at this stage. To make steady progress in the study of seismo-electromagnetic precursors, our group has held that it is primarily important to prove the existence of phenomena at the occurrence of earthquakes (co-faulting signals) and at the arrival of seismic waves (co-seismic signals). Secondarily, it is important that these phenomena be evaluated quantitatively. Therefore, this chapter treats only co-seismic signals in that context.

Our group has used observation sites in northeastern Japan. Figure 1 depicts the locations and operation periods of our observation sites, which were set up on the ground, except at (H) Hosokura site, established *in* the ground. We have observed electric signals using reference electrodes buried in the ground and using condenser-type electrodes insulated from the ground, as described later. We explain co-seismic electric signals detected in (H) Hosokura site in section 2. Then, we describe those detected at other ground surface observation sites in section 3. Thereafter, in section 4, we discuss co-seismic

electric/electromagnetic signals above the ground surface, along with signals detected under and on the ground surface, based on observed data. Finally, we summarize our studies and seismo-electromagnetic phenomena in section 5.

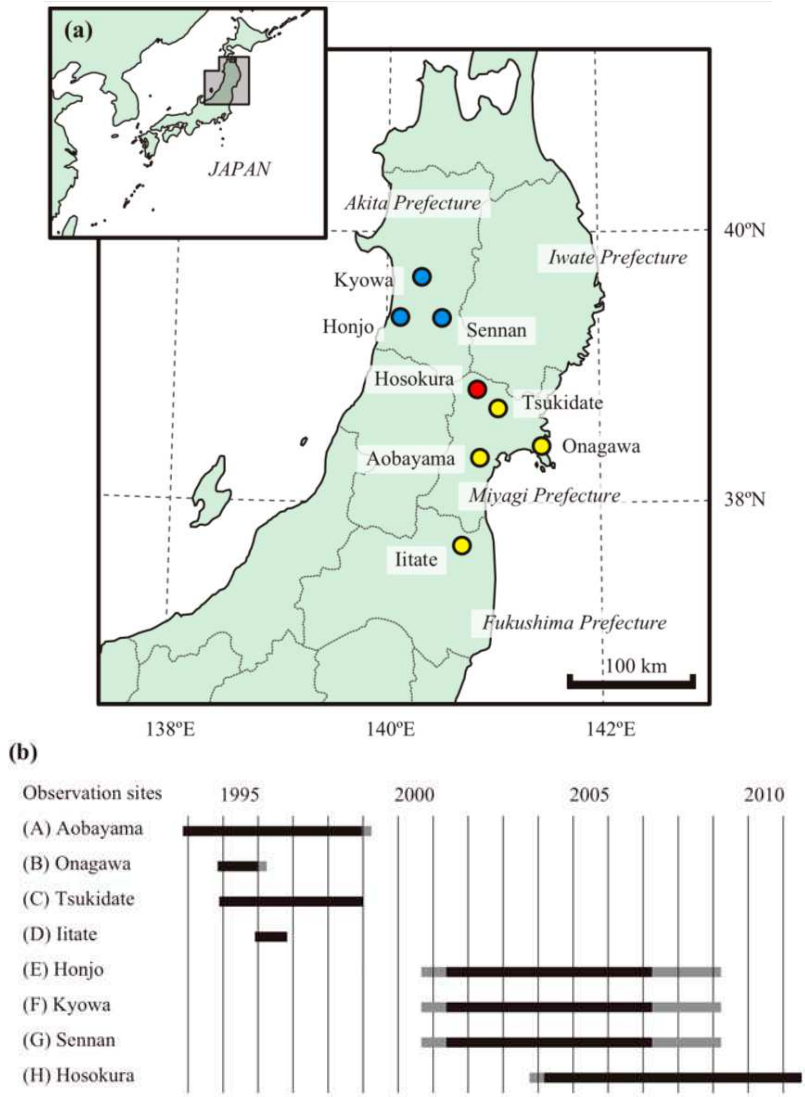

Fig. 1. (a) Locations of observation sites in northeastern Japan. Four yellow circles represent sites on the ground surface in the early stage. Three blue circles show sites on the ground surface in the late stage. The red circle denotes the underground site in the current stage. (b) Operation periods of the sites. Black zones show the period of normal operation. Gray zones show the period of construction, test operation, or bad condition because of superannuation. Only (H) Hosokura site is currently operational

2. Under the ground surface

2.1 Observation site and system

Our underground observation site, (H) Hosokura site (N38°48′, E140°53′), is located in the middle of the main gallery in the Hosokura mine in Miyagi Prefecture, Japan (Figure 1). It intersects sulfide veins in the propylite and green-tuff bedrock (Figure 2a). These rocks are types of hydrothermally altered andesite and tuff, respectively, which are widely distributed throughout northeastern Japan. A shaft near the room connects to the ground surface and galleries including the main one. The lower galleries are flooded. The mine operation has already ceased. However, maintenance continues. The underground water that gushes out is pumped out to maintain the water level at 10 m below the main gallery. It is then chemically treated before discharge. Although the entrances of the room and the main gallery are usually closed, air can leak through openings in the doors. The surface entrance of the shaft is open, and air can pass freely in and out. The observation room is located about 1.5 km from the entrance of the main gallery and about 70 m below the ground surface. The room area is ca. 15 × 12 m^2; its height is ca. 2.5 m (Figure 2b). The air temperature in this room is kept at 23–27 °C year-round using a heater. The air is dusty. The walls, ceiling, and floor are dry, but the main gallery walls are wet.

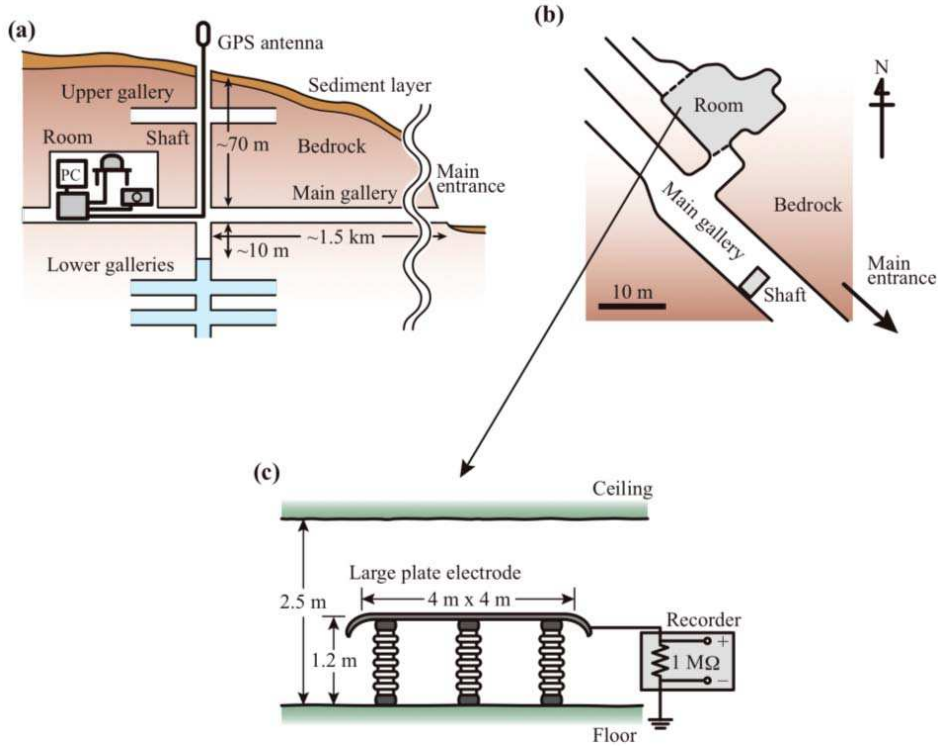

Fig. 2. (a) Side view of (H) Hosokura site in the Hosokura mine. (b) Top view. (c) Observation system in the room. Modified from Okubo et al. (2006) and Takeuchi et al. (2009)

We started observations here with a large plate electrode and a seismometer in 2003 (Okubo et al., 2006a). This large plate-aluminum electrode, with an area of 4 × 4 m^2, and is placed in the middle of the room (Figure 2c) on 15 1.2-m-long ceramic insulators that are terminated at both ends by metal caps. The plate electrode is connected to the floor through a data recorder (DR-1021; TOA-DDK Corp.) with 1-MΩ input impedances on each channel. This electrode functions as a condenser-type sensor with a time constant, probably of the order of ~10^{-4}–10^{-3} s. The seismometer, which is fixed on the floor near the electrode, detects the up-down acceleration of seismic waves. It is also connected to the data recorder.

2.2. Observed signals

Figure 3 presents an example of the observed signals at the arrival of seismic waves. The source earthquake, with magnitude of 4.6, occurred on 27 February 2004. The epicenter (N38°08′, E141°06′) was about 75 km east of this observation site, with focal depth of ca. 70 km. When the S-waves arrived and vertically displaced the room floor, the potential turned rapidly more negative and then reverted gradually to the former background level (Okubo et al., 2006a). The potential superimposed on the background is the potential difference across the internal resistance of the recorder, caused by a transient current, rather than the potential difference between the plate electrode and the floor. Considering the negative-ward shift of the potential and the overall setup of the electrode system, we infer expect the generation of an electric field with its upward electric lines of force. Similar signals were sometimes detected until this electrode system was changed later (Takeuchi et al., 2009).

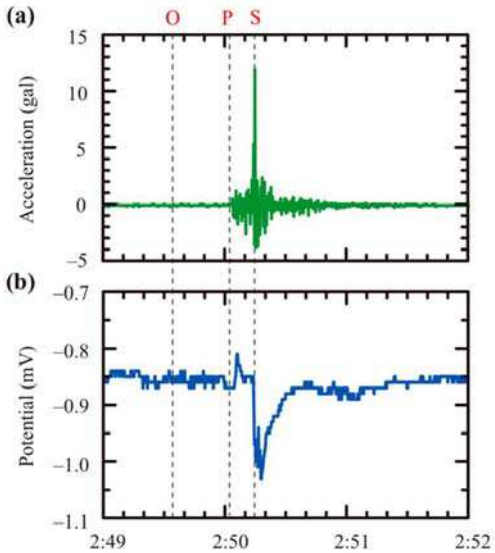

Fig. 3. Examples of electric signals detected at the arrival of seismic waves. (a) Ground up-down acceleration. (b) Electric potential detected by the large plate electrode. "O", "P", and "S" respectively signify the origin time of the earthquake, the time of the P-wave arrival, and the time of S-wave arrival. Modified from Okubo et al. (2006)

As possible mechanisms of the co-seismic signal depicted in Figure 3, we can present four candidates (Okubo et al., 2006a; Takeuchi et al., 2010):

1. **Piezoelectric effect:** Andesite bedrock surrounding the room slightly involves quartz. Therefore, seismic waves cause electric polarizations at each quartz grain/vein, thereby generating an electric field in the room if the summation of the polarizations effectively induces electrification of the floor and walls.
2. **Interfacial electrokinetic effect:** The lower galleries are flooded and the main gallery is wet. Therefore, the bedrock below the room floor will include pore water. When seismic waves push the wet bedrock, the pore water will flow and cause streaming potential because of the interfacial electrokinetic effect. This potential will generate an electric field in the room.
3. **Radon gas:** Radon is widely involved in rocks and soils of various types. When seismic waves arrive, radon gas will emanate from the surrounding bedrock into the room. Radioactive decay of radon gas can increase the air ion concentration. This increment will temporally increase the permittivity of the air and the capacitance of the large plate electrode, which will cause an apparent electromotive force between the electrode and floor if an electric field always exists there.
4. **Positive hole:** In general, igneous rocks subjected to non-uniform loading can activate positive holes (Details are discussed later). When seismic waves arrive, the andesite bedrock will activate positive holes. Positive electrification of the room floor will generate an electric field in the room.

All candidates may occur simultaneously. Their contribution ratios are determined by complex conditions (e.g., the arrival direction of seismic waves, the inhomogeneous bedrock, the wet/dry condition, etc.) and may differ each time. We treat the second candidate again in the next section. In the next subsection, we describe our specific examination of the fourth candidate and verify the positive electrification of the andesite bedrock using laboratory experiments (Takeuchi et al., 2010).

2.3 Laboratory experiments

Figure 4 presents the experimental setup. The rock sample was a block ($4.5 \times 4.0 \times 9.7$ cm^3) quarried from andesite bedrock surrounding the underground observation room. It was air-dried, as was the room floor. The block was placed into an aluminum enclosure, acting as a Faraday cage. The lower volume of the block was loaded uniaxially using a vise equipped with a load cell (CMM1-2T and CSD-819C; Minebea Co., Ltd.). The lower volume was grounded through the vise. Because the lower volume is stressed, its volume expands slightly and pushes the upper unstressed volume upward, which simulates the moment of the arrival of the S-wave frontline, pushing the room floor upward. A conductive tape pasted on the rock top surface is connected to a copper plate immediately below an electric field mill (EF-308T; Tierra Tecnica Corp.). When the top surface is charged, this charge is induced in the plate, thereby creating an electric field toward the sensor of the electric field mill. Consequently, the electric field mill detects the electrification on the sample as a function of the electric field, $q_p = \varepsilon E_d$, where q_p is the surface charge density on the copper plate, ε is the permittivity of air, and E_d is the detected electric field. This electric field mill outputs the 0.8-s averaged E_d for 1 s after signal analysis in 0.2 s. The two series of data are synchronized at the data recorder (8855; Hioki E.E. Corp.). The surface charge density on the

rock top surface q_0 and the electric field on the surface E_0 are calculated using the surface area ratio between the copper plate S_p and the rock top surface S_0.

To minimize the effect of the sample block moving slightly at the application of the first load L from 0 kN, we first kept L = 2 kN for 30–60 min and then started further loading to levels up to 12 kN. Figure 5 portrays some results. The E_0 and p_0 values signify the differences from the values at the initial load L = 2 kN. Positive values denote an electric field with upward electric lines of force, which means that the rock top surface is positively charged. The charge is dissipated with fluctuation after unloading. Similar results were obtained when loading/unloading was repeated at 1–2 hour intervals. Figure 6a shows the plots of E_0 (and p_0) against the maximum load L_{max} applied to the lower block volume. Although the values are scattered, clear correlation exists between the load and electrification. If this trend is extrapolated linearly to 0–2 kN, the respective true values of E_0 and p_0 would be the values shown in the figure plus ca. 0.2 V/m and ca. 2×10^{-12} C/m^2.

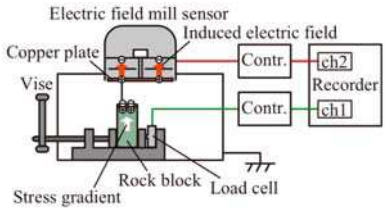

Fig. 4. Setup of non-uniform loading tests using rock blocks. Modified from Takeuchi et al. (2010)

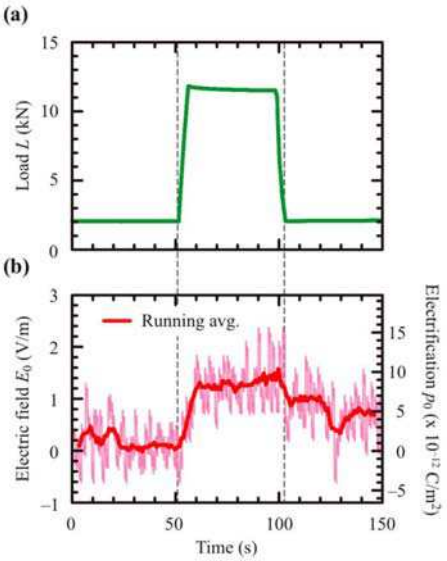

Fig. 5. Typical example of experimental measurements. (a) Loading profile L. (b) Electric field E_0 at the rock top surface and surface charge density calculated as p_0. E_0 and p_0 denote differences from the values at the initial load L = 2 kN. Modified from Takeuchi et al. (2010)

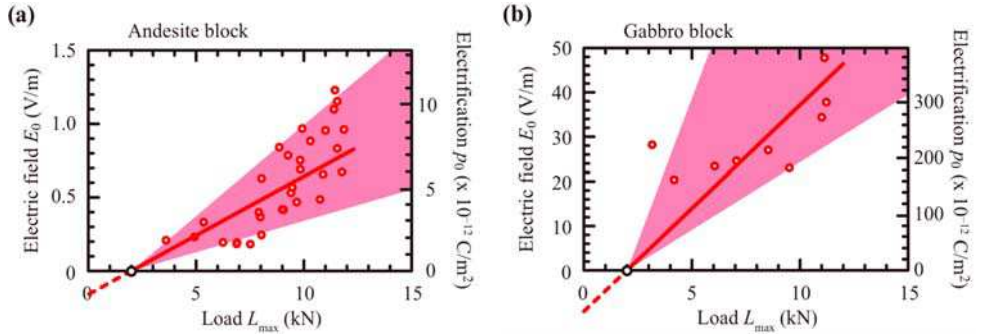

Fig. 6. Electric field E_0 and electrification p_0 measured on the top surface of the upper unstressed volume of the rock block shown against the maximum load L_{max} applied to the lower volume of the rock. (a) Quartz-bearing andesite. (b) Quartz-free gabbro. E_0 and p_0 denote differences from the values at the initial load L = 2 kN. Modified from Takeuchi et al. (2010)

The andesite under study involves some quartz. Therefore, we should consider first the piezoelectric effect as the cause of the signals detected in the laboratory. Here, we conducted similar experiments with a quartz-less gabbro block (9.4 × 2.0 × 9.7 cm^3) as a control. Results show that the gabbro showed the same electric field and electrification, even more intensely than the andesite (Figure 6b), which implies that the piezoelectric effect of quartz is not the prime cause of the signals detected in the laboratory. Randomly oriented piezo-dipoles in the andesite block would be canceled by one another. The interfacial electrokinetic effect of pore water is secondarily considered as the cause of the signals detected in the laboratory. However, we can also discount this effect because the samples were well air-dried. Now, we expect the stress-activation of positive holes (Takeuchi et al., 2010).

Minerals that form igneous rocks, including andesite, generally involve peroxy bonds that are ubiquitous lattice defects (O_3X–OO–YO_3 with X, Y = Si^{4+}, Al^{3+}, etc.). Figure 7 shows an example of an energy level of the peroxy bond in the case of quartz. The unoccupied $3\sigma_u^*$ level usually lies in the forbidden band (Figure 7a). When the lattice structure around this bond is mechanically deformed, the energy level shifts downward and becomes an accepter (Figure 7b). As an electron jumps in from a neighboring oxygen anion (O^{2-}), a hole appears at this site (Figure 7c), which is a positive hole whose state (O^-) can move through the valence band like charge carriers moving in any p-type semiconductor material (Figure 7d). This mechanism can construct a model below to explain the signals detected in the laboratory. When we stressed the lower volume of the andesite/gabbro block, positive hole charge carriers were activated in the volume. Positive holes attempted to diffuse into the upper unstressed volume and were simultaneously attracted electrically by electrons trapped at peroxy bonds. Consequently, an electric unevenness, i.e. an electric polarization, was formed in the lower volume. This polarization and a small part of the holes reaching the top surface charged the surface positively. As the load was released, positive holes slowly dissipated and recombined with electrons. As a result, the polarization and electrification dissipated with fluctuations.

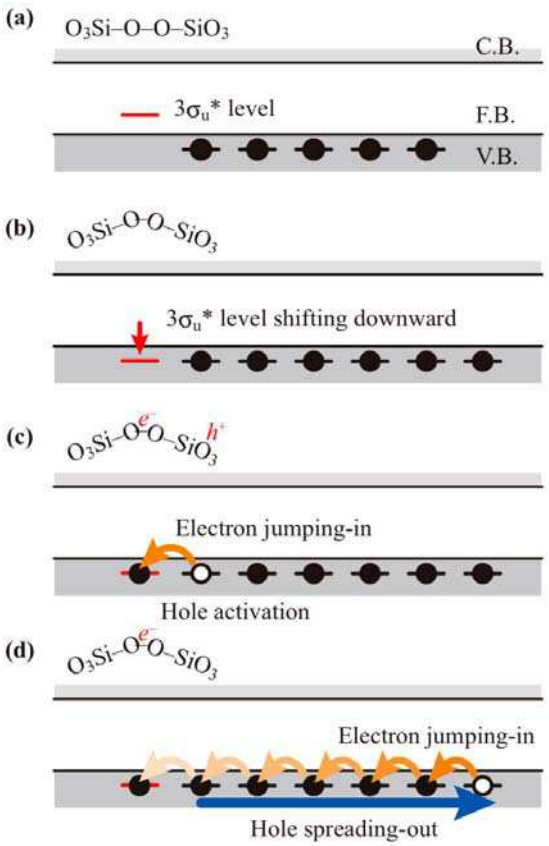

Fig. 7. Band model of stress-activation of a positive hole in the case of quartz. (a) Normal state. (b) Downward shift of the unoccupied $3\sigma_u^*$ level accompanying structure deformation around a peroxy bond under subjection of a load. (c) Jump-in of an electron and activation of a positive hole. (d) Movement of a positive hole through the valence band by successive electron-hopping steps. Modified from Takeuchi et al. (2010)

2.4 Short discussion

The stress activation of positive holes will occur also in the andesite bedrock surrounding the underground observation room at the arrival of seismic waves because the basic mechanism of activation and movement of positive holes is expected to be similar in the observation sites and laboratory. Considering the electrode system simplified as portrayed in Figure 2c, the transient current I_{ts} passing through the internal resistance of the recorder R_{in} during arriving of S-waves is given as $I_{ts} = (V_{rec} - V_{bkg})/R_{in}$, where V_{rec} is the recorded potential and V_{bkg} is the background level. Integration with time gives the charge induced on the electrode as ca. 10^{-9} C and its surface density as ca. 10^{-10} C/m^2. These values are larger than those obtained from laboratory experiments, but we should consider differences in conditions such as the stressed volume, the applied stress, the stress rate, etc.

3. On the ground surface

3.1 Observation sites and systems

Our observation sites on the ground surface in the early stage were located in Miyagi and Fukushima Prefectures, Japan (Figure 1).

(A) **Aobayama** (N38°15′, E140°50′): This site was located in a growth of miscellaneous trees in the middle of a slight slope toward a mountain stream on the Aobayama Campus of Tohoku University. Figure 8a shows the four pairs of reference electrodes (RE-5; M.C. Miller Co. Inc.) horizontally and vertically buried in the ground (Takeuchi et al., 1995, 1997a). Electric signals were transported to a pen-recorder with a 10-Hz low-pass filter through coaxial cables. Thereafter, the A/D converted data were stored on the HD of a PC at 1 Hz sampling. Figure 8b presents another system built later (Takeuchi et al., 2000). A pair of reference electrodes (RE-5; M.C. Miller Co. Inc.) was buried vertically with a 2-m distance separating them. A dodecagonal plate electrode (3 m diameter) was placed on 3 1.5-m-long ceramic insulators about 50 m from the electrodes. The plate electrode was connected to the ground through a data recorder. A seismometer was fixed on the floor of an observation room nearby. All electric signals were transported to the data recorder through coaxial cables. A PC stored the A/D converted data from the recorder at 100 Hz only from 5-s before the seismic trigger to 3-min after the trigger. This site was operational during October 1993 – March 1999.

(B) **Onagawa** (N38°26′, E141°29′): This site was located at the site of the Onagawa geomagnetic field observatory of Tohoku University, about 80 m from a cliff facing the Pacific Ocean (Takeuchi et al., 1997b). Two pairs of reference electrodes (RE-5; M.C. Miller Co. Inc.) were used. One pair was buried horizontally with a 40-m separation distance in the N-S direction at 0.5 m depth. Another was buried vertically at 0.5 m and 1.5 m depths. All electric signals were transported to a pen-recorder with a 10-Hz low-pass filter through coaxial cables. Thereafter, the A/D converted data were stored on the HD of a PC at 1 Hz sampling. This site was operational during October 1994 – March 1996. Electric shocks from lightning frequently halted data recording.

(C) **Tsukidate** (N38°43′, E141°02′): This site was located in the campus of Tohoku-Polytechnic College, ca. 10 m from nearby a college building (Takeuchi et al., 1997b). The ground level of the college buildings had been raised. There was one pair of reference electrodes (RE-5; M.C. Miller Co. Inc.) buried vertically at 7 m and 10 m depths. All electric signals were transported to a pen-recorder with a 10-Hz low-pass filter through coaxial cables. Thereafter, the A/D converted data were stored on the HD of a PC at 1 Hz sampling. This site was operational during December 1994 – December 1998. However, data have included strong pulses since March 1995 because of construction work on a new building ca. 10 m from the electrodes.

(D) **Iitate** (N37°42′, E140°40′): This site was located at the site of the Iitate telescopic observatory of Tohoku University, far from densely populated areas. Figure 9 portrays locations of five reference electrodes (RE-5; M.C. Miller Co. Inc.) buried vertically and horizontally in the ground (Takeuchi et al., 1997b). All electric signals were transported to a pen-recorder with a 10-Hz low-pass filter through coaxial cables. Thereafter, the A/D converted data were stored on the HD of a PC at 1 Hz sampling. This site was operational during November 1995 – November 1996. However, the system was often unstable and stopped data recording.

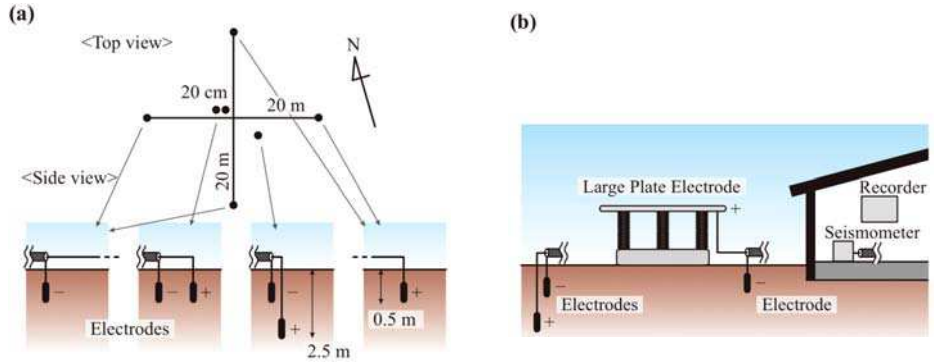

Fig. 8. (a) Observation system of (A) Aobayama site in the early stage. (b) System in the late stage. Modified from Takeuchi et al. (1995, 2000)

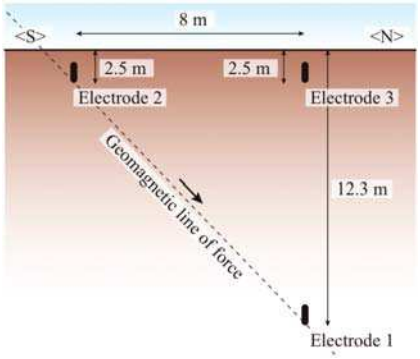

Fig. 9. Observation system of (D) Iitate site. Modified from Takeuchi et al. (1997b)

During these 5-year observations, it was confirmed that no electric signal was generated by minute displacements of the electrodes buried in the ground or by vibration of the coaxial cables. These sites detected electric signals with the waveform of damped oscillations at the arrival of seismic waves. Especially, (A) Aobayama site was so sensitive that it detected electric signals at the arrival of very weak seismic waves from a M7.6 earthquake that occurred in 1994, ca. 550 km below Vladivostok, Russia (Takeuchi et al., 1995, 1997a) and from the M7.2 Kobe earthquake that occurred in 1995, ca. 600 km from this site (Okubo et al., 2005). To minimize the effects of artificial noises overlapping the natural electrotelluric currents flowing horizontally, the vertically buried electrode pairs were more useful than those buried horizontally. Moreover, the vertical signals were 10 times stronger than the horizontal signals (Okubo et al., 2005). Based on these experiences, in the next stage, we selected burial of the electrode pairs vertical in the ground and renewed three observation sites in Akita Prefecture, Japan (Figure 1). The systems at each site were very similar. Hereinafter, we mainly treat observation data obtained at the three sites as described below.

(E) Honjo (N39°23′, E140°04′): This site was located in a green belt on the Honjo Campus of Akita Prefectural University, which is surrounded by rice fields (Okubo et al., 2006b). No tall building existed around this site. Figure 10 depicts an outline of the system. One

pair of reference electrodes (RE-5; M.C. Miller Co. Inc.) was buried vertically at 0.5 m and 2.5 m depths. A large aluminum plate electrode, with 4 × 4 m² area, was supported by five insulators at a height of about 4 m. The plate electrode was connected to the ground through a data recorder (DR-1021; TOA-DKK Corp.) with 1-MΩ input impedances on each channel. All electric signals were transported to the data recorder through coaxial cables. A PC controlled the recorder and stored data on its HD at 4 Hz. The data clock was synchronized to within 1 ms of the time accuracy using a GPS unit. Before starting ordinal observations, the large plate electrodes were tested under various weather conditions (e.g., heavy snow) from August 2000. Although the system functioned well in 2001–2006, the electrodes became too old to use in 2007. It became difficult to maintain and repair them. Therefore, we dismantled them in 2009.

(F) **Kyowa** (N39°40′, E140°23′): This site was located in a garden yard of a small recreation house of Akita Prefectural University (Okubo et al., 2006b) in a sparsely populated area. The system was identical to that of (E) Honjo site, as shown in Figure 10, except for the sampling rate: 10 Hz. The operation period was identical to that of (E) Honjo site.

(G) **Sennan** (N39°23′, E140°30′): This site was located on the sports ground of a former primary school surrounded by rice fields (Okubo et al., 2006b). No tall building existed around this site. The system resembled that at (F) Kyowa site. In addition to the two types of electrodes, this site had a seismometer (L-22D; Mark Products) fixed on the floor of the observation room nearby to detect the up–down component of the ground surface velocity, as shown in Figure 10. The operation period was identical to those of (E) Honjo and (F) Kyowa sites.

Hereinafter, we designate the electric signal detected between the pair of reference electrodes as "Earth potential difference (EPD)" and designate the electric signal detected between the large plate electrode and the ground as "atmospheric electricity (AE)".

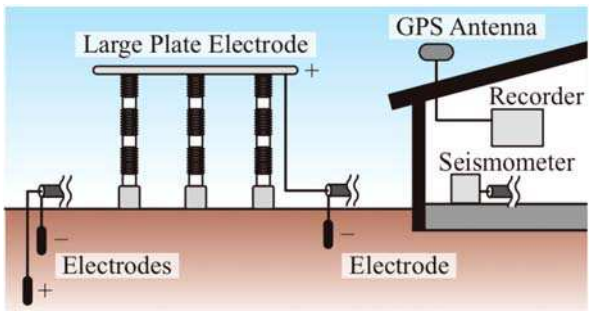

Fig. 10. Observation system of (E) Honjo, (F) Kyowa, and (G) Sennan sites. The seismometer was set up only at (G) Sennan site. Modified from Okubo et al. (2004)

3.2 Observed signals

A M6.3 earthquake occurred near the boundary between Iwate and Miyagi Prefectures at 13:02 on 2 December 2001, UT. The epicenter was (N39°23′, E141°16′). The focal depth was 130 km, which was extremely large relative to the distances among the three sites in Akita Prefecture, as were the hypocentral distances of the sites. Therefore, the local seismic intensities at the sites were similar.

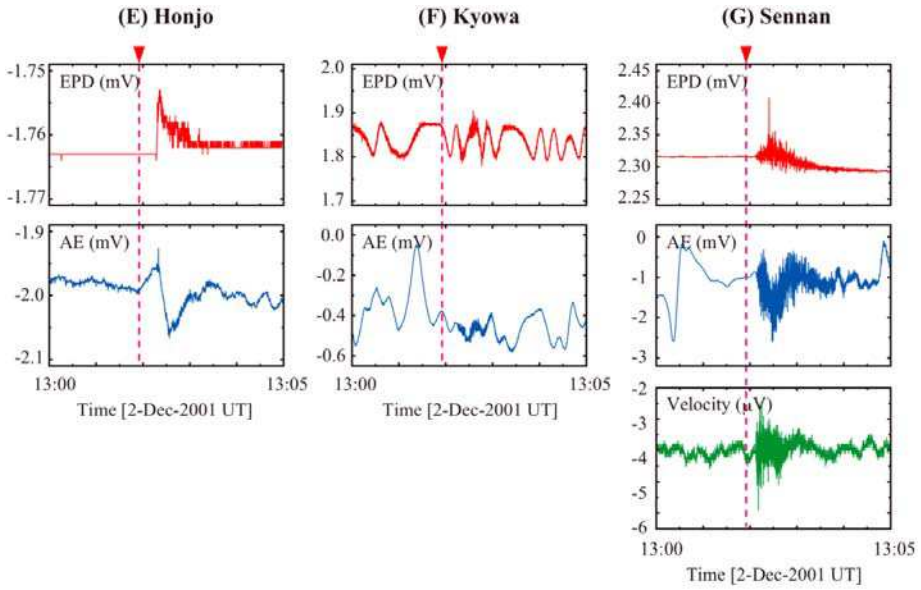

Fig. 11. Raw data recorded before and after the arrival of seismic waves at (E) Honjo, (F) Kyowa, and (G) Sennan sites. The seismometer was set up only at (G) Sennan site. Modified from Okubo et al. (2004)

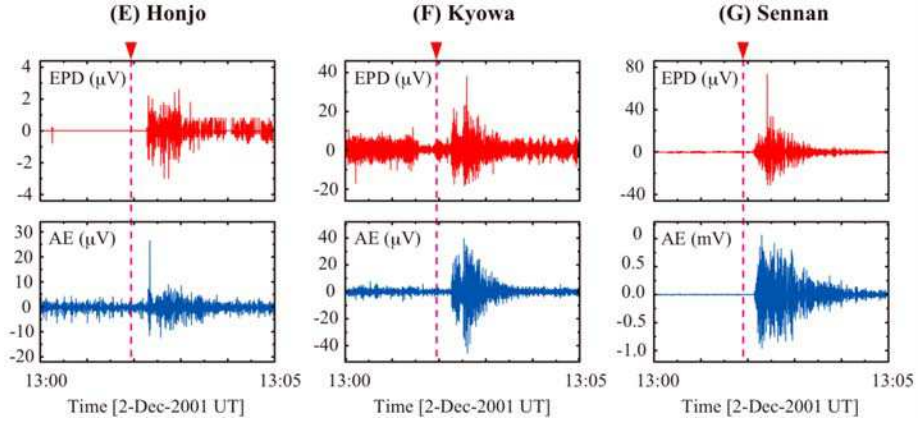

Fig. 12. Signals extracted from raw data presented in Figure 11 using the 1-s moving average method. Modified from Okubo et al. (2004)

Figure 11 portrays plots of raw data obtained before and after the arrival of seismic waves at respective sites. The upper rows show the EPD signal, the middle ones show the AE signal, and the lower one, only that for (G) Sennan site, shows the ground velocity. Dotted lines show the origin time of the earthquake. Signal oscillations are confirmed, although some are small against the background variations. To clarify the signals that we examined specifically, we adopted the moving average method. A time period of 1 s was used for

calculation of the moving average. The original data were subtracted by the 1-s moving averages. Then the signals were extracted as shown in Figure 12. The EPD and AE signals with the waveform of damped oscillations are induced simultaneously at the arrival of seismic waves, although some still include high background noise. The waveforms of EPD and AE signals are similar to that of the up–down velocity in (G) Sennan site. The waveforms at (E) Honjo and (F) Kyowa sites will also probably resemble those of the local velocity.

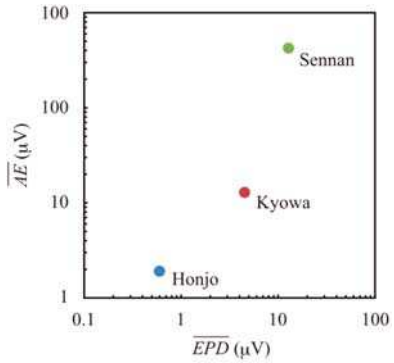

Fig. 13. Positive relation between the average of the earth potential difference ($\overline{EPD}$) and the average of the atmospheric electricity ($\overline{AE}$). Modified from Okubo et al. (2004)

Figure 13 shows the relation between the average amplitudes (AA) of the extracted EPD and AE signals, defined as

$$AA = \sqrt{\frac{1}{30(\text{sec})} \sum_{\text{peak time}(t=0(\text{sec}))}^{t=30(\text{sec})} (signal + background(t))^2} - \sqrt{\frac{1}{30(\text{sec})} \sum_{\text{no propagation}(t'=0(\text{sec}))}^{t'=30(\text{sec})} (background(t'))^2} \quad . \tag{1}$$

The summation in the first root is over a period of 30 s after the peak time of the extracted EPD and AE signals; another in the second root is over a period of 30 s when no seismic wave propagated. Hereinafter, we respectively designate the AA of the extracted EPD and AE signals as "$\overline{EPD}$" and "$\overline{AE}$". Figure 13 portrays a positive relation between $\overline{EPD}$ and $\overline{AE}$. Although the local seismic intensity is similar among the three sites described above, the $\overline{EPD}$ and $\overline{AE}$ at (E) Honjo site are smaller and those at (G) Sennan site are larger.

The (G) Sennan site was more sensitive than the other two sites in Akita Prefecture. It detected EPD and AE signals at the arrival of seismic waves from smaller earthquakes occurring in and around Akita Prefecture (Okubo et al., 2007). For example, the left columns in Figure 14 show plots of data obtained before and after the arrival of seismic waves from a M6.2 earthquake that occurred 12 km below the coast of Miyagi Prefecture at 22:14 on 25 July 2003, UT. To clarify the EPD and AE signals that we specifically investigated, we adopted the digital natural observation (D-NOB) method this time. This method is an analytical method used as a novel technique for signal analysis. Details of the concept and method are provided in the Appendix. The EPD and AE signals were extracted as shown in

the right columns in Figure 14. Now it is clear that EPD and AE signals with the waveform of damped oscillations are induced simultaneously at the arrival of seismic waves. The waveforms of the EPD and AE signals resemble that of the ground up-down acceleration. These extracted waveforms resemble those presented in Figure 12.

Figure 15 shows relations among $\overline{EPD}$, $\overline{AE}$, and the average of amplitude of the up-down acceleration "$\overline{ACC}$" also obtained from Eq. 1 for earthquakes occurring in and around Akita Prefecture in 2003. The $\overline{EPD}$ is linearly related with $\overline{ACC}$ and has a roughly linear relation with $\overline{AE}$.

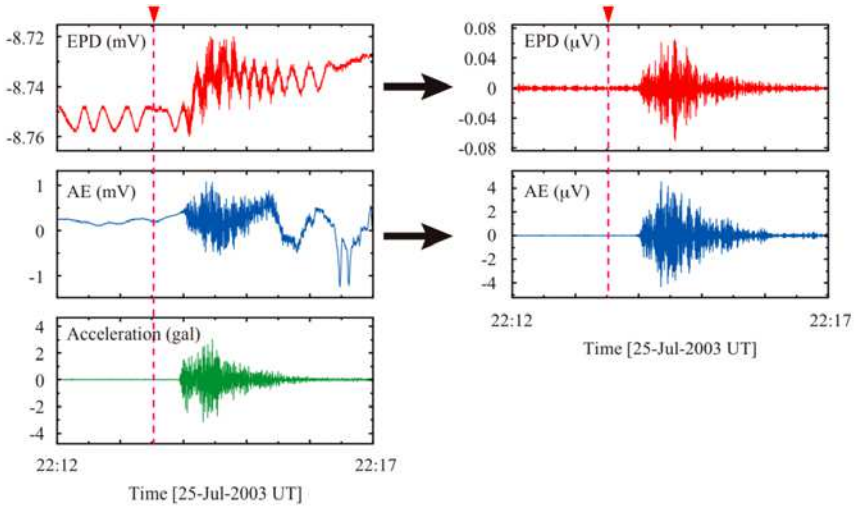

Fig. 14. (Left columns) Observation data recorded before and after the arrival of seismic waves at (G) Sennan site. (Right columns) Signals extracted from observation data in the left columns using the D-NOB method. Modified from Okubo et al. (2007)

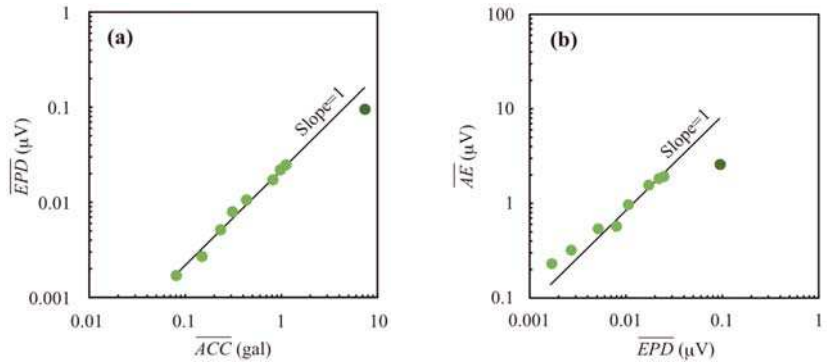

Fig. 15. (a) Positive relation between the average of the earth potential difference ($\overline{EPD}$) and the average of the ground up-down acceleration ($\overline{ACC}$). (b) Positive relation between the average of the atmospheric electricity ($\overline{AE}$) and $\overline{EPD}$. Linear lines with the slope of 1 are obtained from the plots, excluding the dark plots. Modified from Okubo et al. (2007)

3.3 Generation mechanisms

First, we discuss possible generation mechanisms of EPD signals. As possible mechanisms, we can list the four candidates again:

1. **Piezoelectric effect:** The soil at the observation sites includes quartz grains. Therefore, seismic waves cause electric polarization at each grain, which will generate an electric field in the soil if the summation of the polarizations is sufficiently large under a certain convenient condition. However, because piezoelectric polarizations at each quartz grain in the soil will generally be so small and random, its vector summation will be almost negligible. Therefore, this candidate is discounted as the prime factor.
2. **Interfacial electrokinetic effect:** The soil, at least deeper soil, generally includes pore water. When seismic waves push the wet soil, the pore water will flow and cause streaming potential as a result of the interfacial electrokinetic effect. This potential will generate an electric field in the soil.
3. **Radon gas:** Radon is widely distributed in rocks/soils of various types. When seismic waves arrive, radon gas will emanate from the ground. Radioactive decay of radon gas can increase the air ion concentration. This increment will increase the permittivity of the air and the capacitance of the large plate electrode, which will produce an apparent electromotive force between the plate electrode and the ground surface, both exposed to the vertical atmospheric electric field. Consequently, AE signals appear. However, radon gas cannot explain EPD signals.
4. **Positive hole:** In general, soils include mineral grains from igneous rocks. When seismic waves arrive, positive holes will be activated in the grains. An electric unevenness by mobile positive holes and trapped electrons will generate an electric field in the soil. However, if the soil is wet, then pore water may absorb the charges (Balk et al., 2009).

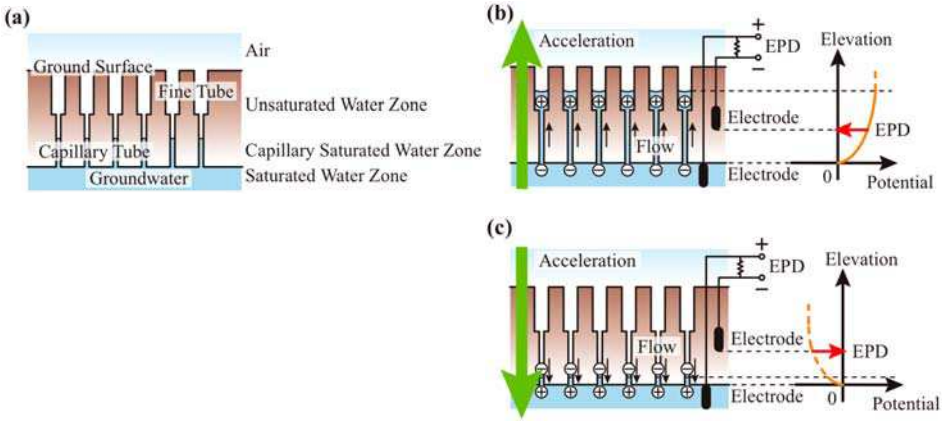

Fig. 16. Generation mechanism of the Earth potential difference (EPD) signals in a geohydraulic model. (a) Model of the near-surface soil layer from the viewpoint of water-saturation/unsaturation. (b) Negative EPD signal induced by streaming potential because of the upward flow of water along the tubes. (c) Positive EPD signal induced by streaming potential because of the downward flow of water along the tubes. Modified from Okubo et al. (2005)

All candidates may simultaneously cause phenomena. Their contribution ratios will be determined by complex conditions (e.g., the arrival direction of seismic waves, inhomogeneous bedrock, wet/dry conditions, etc.) and may be different each time. However, a linear relation exists between the $\overline{EPD}$ and $\overline{ACC}$ at (G) Sennan site, as depicted in Figure 15. Moreover, in those observations, the EPD waveform resembles that of the ground up-down acceleration. Therefore, the force applied to pore water varies similarly to the EPD waveform. These results demonstrate that the amplitude of EPD signals increases proportionally with the pressure difference applied to pore water. Consequently, in this section, we specifically examine the second candidate (interfacial electrokinetic effect) and propose a detailed model for EPD signals.

From the viewpoint of geohydraulics, the water content generally increases with increased depth in the near-surface soil layer with pores. The upper region is called the unsaturated water zone; the lower one is the saturated water zone (Smith, 1982; McCarthy, 2006). Here, we consider only the vertical component. Figure 16a portrays a network model of pores in the near surface soil layer as a bundle of tubes connecting the air and the saturated water zone. The upper part of the tubes is fine and the lower part has capillaries. The lower part of the capillary tubes maintains the pore water, named the capillary saturated water zone. The lower part of this system is the saturated water zone, where the network of pore water is completely connected. Negative ions adhere to the inner wall of the tubes, so that positive ions are predominant in the capillary water. This engenders the formation of electric potential difference between the center and wall of the tubes: the so-called zeta-potential.

Based on early observations and theoretical work, a close coupling dynamics is well known to exist between the seismic acceleration and the pore pressure or water level (Muire-Wood and King, 1993; Kano and Yanagidani, 2006; Yan et al., 2008). This coupling dynamics must be valid in our geohydraulic system presented in Figure 16a. As portrayed in Figure 16b, when acceleration is inflicted upward in this system, the water in the capillary tubes flows upward along the tubes. This water is positively charged. Therefore, flowing up of the water leads to positive electrification in the upper range of the tubes. However, the lower range of the tube charges is negative. Consequently, vertical electric polarizations are formed and an electric potential difference (called streaming potential) appears between the upper level of the water flowing up and the saturated water zone. No more charge exists above the upper level of the water. Therefore, the electric potential in this range is almost constant under an ideal condition. When the positive and negative terminals of electrodes are buried respectively in the saturated water zone and the unsaturated water zone, they will detect a negative EPD signal. As Figure 16c shows, when acceleration is inflicted downward in this system, the opposite phenomenon occurs and the electrode will detect a positive EPD signal. Consequently, when seismic waves induce vertical oscillation of this geohydraulic system, the electrodes detect EPD signal oscillation.

Next, we propose an AE signal generation mechanism. We first consider the apparent AE signals because of vibration of the large plate electrodes. However, if so, then the three plate electrodes with identical setup would show AE signals with equal (or equivalent) amplitude. This is contrary to the result portrayed in Figure 13. As Figures 12 and 14 show, the AE signal oscillation appears along with the EPD signal oscillation. Moreover, as shown in Figures 13 and 15, the $\overline{AE}$ exhibits a good positive relation with $\overline{EPD}$. Therefore, the generation mechanism of AE signals must couple with that of EPD. Figure 17 presents a schematic of a

possible mechanism of AE signals. As shown in Figure 16, streaming potential oscillation appears in the unsaturated water zone. This oscillation is equivalent to the electric polarization oscillating vertical to the ground immediately under the ground surface. Their charges on the ground surface generate an atmospheric electric field vertical to the ground. Consequently, an electric potential appears between the large plate electrode and the ground surface. Charges move between the electrode and the ground via the input impedance of the recorder to cancel the potential difference oscillation, which is detected as an AE signal oscillation.

Actually, similarly oscillating AE signals are often detected at (H) Hosokura site in addition to the AE signal shown in Figure 3b in section 2. Although the floor of the underground observation room is dry, the andesite bedrock below the floor will involve pore water. When seismic waves induce oscillation of the capillary water, the induced streaming potential will generate the vertical electric field oscillating in the room.

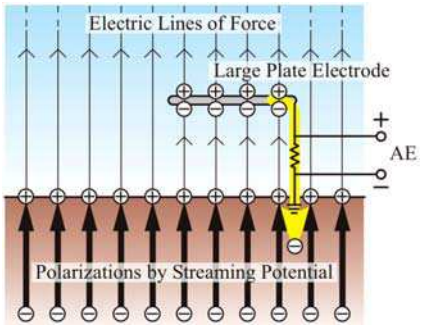

Fig. 17. Generation mechanism of the atmospheric electricity (AE) signals coupled with generation of streaming potential in the near-surface soil layer. Modified from Okubo et al. (2004)

3.4 Short discussion

According to the geohydraulic system shown in Figure 16, the EPD signal amplitude is expected to depend on the electrode positions. We assume six cases as shown in Figure 18.

a. When both electrodes are located horizontally parallel to each other in the unsaturated water zone (Figure 18a), EPD signals will be very small. Even if streaming potential appears at the electrodes, the potential difference between them will be small. For example, at (A) Aobayama site, the vertical EPD signal was 10 times larger than the horizontal one, in which each electrode was separated 2 m (Takeuchi et al., 1995, 1997a).
b. When one electrode is located in the unsaturated water zone and another is in the saturated water zone (Figure 18b), EPD signals will be large. The electrode pair is located at both ends of electric polarization because of streaming potential. Therefore, EPD takes the maximum.
c. When both electrodes are located in the saturated water zone (Figure 18c), EPD signals will be very small. The pore water network is completely connected. Therefore, this zone is sufficiently conductive and most streaming potential is canceled. In fact, at (A) Aobayama site, two electrodes at 10 m and 12 m depths, both probably in the saturated water zone, detected extremely small EPD signals (Takeuchi et al., 1995, 1997a).

d. When one electrode is located deeply in the unsaturated water zone and another is deeply in the saturated water zone (Figure 18d), EPD signals will be large. This case acts like case (b). For example, at (C) Tsukidate site, a pair of electrodes was buried at 7 m and 10 m depths. A borehole survey confirmed that the upper level of the saturated water zone was at 9 m depth. This site detected sufficiently large EPD signals against background variations (Takeuchi et al., 1995, 1997a, 1997b).
e. When both electrodes are located in the unsaturated water zone far from the deep saturated water zone (Figure 18e), EPD signals will be very small. No pore water flows up in the upper range of the thick unsaturated water zone. Therefore, little potential difference exists between the electrodes.
f. When one electrode is in the unsaturated water zone and another is near the saturated water zone (Figure 18f), EPD signals will not be so large. Until the lower electrode is submerged in the water flowing up, no significant potential difference exists between the electrodes.

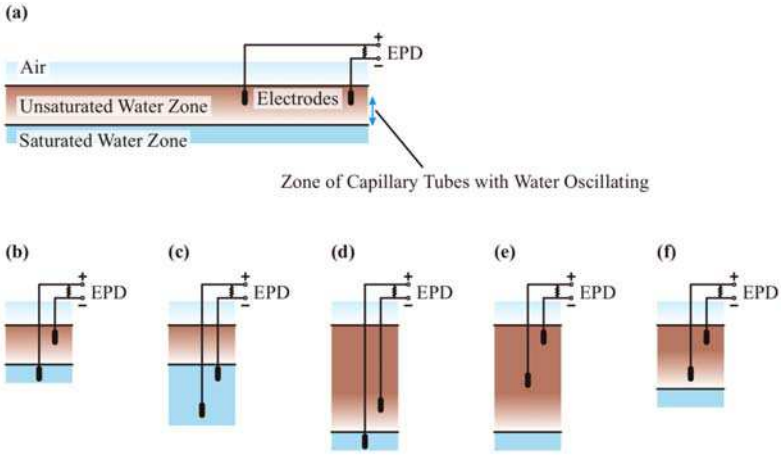

Fig. 18. Six cases of locations with the electrode pair buried and the saturated/unsaturated water zone levels. (a) Both electrodes are horizontally parallel to each other in the unsaturated water zone. (b) One electrode is in the unsaturated water zone; another is in the saturated water zone. (c) Both electrodes are in the saturated water zone. (d) One electrode is deeply situated in the unsaturated water zone; another is deeply situated in the saturated water zone. (e) Both electrodes are in the unsaturated water zone far from the deep saturated water zone. (f) One electrode is in the unsaturated water zone; another is near the saturated water zone. Modified from Okubo et al. (2005)

The significant difference of the $\overline{EPD}$ among the three sites in Akita Prefecture probably results from the difference in position of the buried electrodes and the saturated water zone.

(E) Honjo site was 6 m above the surrounding rice fields. The saturated water zone is expected to be a few meters deeper than the fields. Therefore, this site corresponds to case (e); the $\overline{EPD}$ was small.
(F) Kyowa site was on a flat land in the middle of mountains. Therefore, this site corresponds to case (f); the $\overline{EPD}$ was not so large.

(G) Sennan site was on the same level as the surrounding rice fields. The saturated water zone is expected to be a few meters deeper than the fields. Therefore, this site corresponds to case (b); the $\overline{EPD}$ was large.

4. Above the ground surface

According results of our laboratory experiments, as described in Section 2, when a large volume of dry igneous rock appears on the ground surface, a vertical atmospheric electric field will arise from positive holes activated on the ground surface at the arrival of seismic waves. Additionally, according to our geohydraulic system, as shown in Figures 16 and 17, greater ground acceleration can cause a larger charge density on the ground surface under a certain condition of the saturated/unsaturated water zones, as in case (b) of Figure 18, which engenders a larger atmospheric electric field vertical to the ground surface. This case will correspond to (G) Sennan site. However, the charge density on the ground surface cannot be large in case (e) of Figure 18 because part of the electric field vertical to the ground will be absorbed in the thick upper unsaturated water zone, which engenders a decrease of the charge density on the ground surface and a small AE signal. This case corresponds to (E) Honjo site.

If the surface charge induced on the ground surface is sufficiently large to cause corona discharge in the atmosphere, say ca. 5×10^{-5} C/m^2 (Lockner et al., 1983), then it may be detected as earthquake lightning. If the amplitude of the vertical atmospheric electric field induced by the surface charges is sufficiently large above a large area, say ca. 1 kV/m (Pulinets et al., 2000; Rapoport et al., 2004), then it may even disturb plasma in the ionosphere with detectable amplitudes. The amplitude of this field depends not only on the seismic wave amplitude but also on the underground water condition. Therefore, there is no guarantee that this field is strongest above the epicenters. This electric field will form from the epicenter. Therefore, no guarantee exists that the influence of this field on ionospheric disturbances is strongest at the epicenter.

However, such disturbances will be overwhelmed in further strong disturbances coming later. They are detected as abnormal changes in the total electron content obtained from analyses of GPS signals, so-called GPS-TEC (Liu et al., 2010; Rolland et al., 2010; Galvan et al., 2011). The most widely accepted causes of such GPS-TEC anomalies are Rayleigh waves and tsunamis. Their vertical motion triggers acoustic gravity waves in the neutral atmosphere. These waves reach the ionosphere in 6–7 min and interact with plasma in the ionosphere. Moreover, the flow of the tsunami, which is a conductive mass moving in a magnetic field, generates a surrounding weak secondary magnetic field because of magnetohydrodynamic interaction (Tyler, 2005). We defer to other reports in the literature for details because such postseismic phenomena are beyond the scope of this chapter.

5. Summary

To make steady progress in the study of seismo-electromagnetic precursors, our group has believed that it is important, first of all, to prove the existence of co-faulting and coseismic phenomena. In accordance with our beliefs, we built observation sites on and in the ground (intermittently 8 sites in total) and have observed electric signals with (1) pairs of reference electrodes in the ground for EPD signals, (2) condenser-like plate electrodes insulated from

the ground for AE signals, and/or (3) seismometers at some sites. As a result, we gained the following knowledge related to the signals.

1. **In the early stage** (on the ground surface): Results showed that EPD and AE signals were generated at the arrival of seismic waves. Their amplitudes were positively related with the local seismic intensity. The vertical amplitude of EPD was 10 times larger than the horizontal amplitude.
2. **In the late stage** (on the ground surface): We again detected EPD and AE signals. We extracted weak signals from the background fluctuation using the moving average method and the D-NOB method. We evaluated their amplitudes, which showed that $\overline{EPD}$ and $\overline{ACC}$ were linearly related and $\overline{EPD}$ and $\overline{AE}$ were roughly in a linear relation. We proposed their generation models based on streaming potential caused by vertically oscillating pore water.
3. **In the current stage** (under the ground surface): We detected electric signals probably because of the generation of a vertical electric field in the underground room. We expected positive electrification of the floor as a possible cause. We conducted non-uniform loading tests in a laboratory using a rock block quarried from the site and verified the positive electrification.

Our studies described in this chapter represent great advancement for the steady progress of the study of seismo-electromagnetic precursors. The next step, we think, is to understand the dynamic electric and electromagnetic fields in the ground further. To do so, it is necessary to set up multiple observation sites under, on, and above the ground surface simultaneously, which can detect three-dimensional dynamic electric and electromagnetic phenomena from focal zones. Unfortunately, our observation sites on the ground surface are no longer in operation. However, we developed the underground observation site, (H) Hosokura. Now this site has various other sensors: an electric field mill, two air ion counters (for positive and negative ions), an air temperature-humidity probe, reference electrodes, and two fluxgate magnetometers (Takeuchi et al., 2009; Okubo et al., 2011).

Finally, we summarize electric and electromagnetic (and magnetic) phenomena described in this chapter as shown below.

a. **Preseismic signals:** Quasi-static electromagnetic changes appear from the focal zone before its failure (Figure 19a). We can predict earthquakes if we can detect them with conviction. However, detection of such direct signals with scientific evidence is extremely rare. One reason is probably that their amplitude is extremely small. Another is that these changes probably cannot penetrate the water-saturated near-surface sediment layer. Placing observation sites below the layer, like (H) Hosokura site, will support the detection of these signals. Although some reports in the literature describe ionospheric disturbances occurring before earthquakes (Hayakawa et al., 2010; Oyama et al., 2008), we defer to the literature for details because such preseismic phenomena are beyond the scope of this chapter.
b. **Co-faulting signals:** Quasi-static electromagnetic changes, probably with further strong amplitudes, appear from the focal zone during failure (Figure 19b). Although detection of such direct signals using scientific evidence is very rare, probably for the reasons described above, one report describes that fluxgate magnetometers at (H) Hosokura site detected changes in the geomagnetic field during failure (Okubo et al., 2011). On the other hand, seismic waves induce pore water oscillation in the near-surface sediment

layer and cause the streaming potential. Formation of the vertical atmospheric electric field caused by the streaming potential starts spreading out from the epicenter in association with seismic wave propagation. Moreover, a tsunami is generated and gravity waves spread upward.

c. **Coseismic signals:** Local electric and electromagnetic phenomena are generated under, on, and above the ground surface at the arrival of seismic waves (Figure 19c). This chapter specifically addresses these signals. The streaming potential is generated in the near-surface sediment layer; the vertical atmospheric electric field is generated above the ground. They are detected as EPD and AE signals. On the other hand, gravity waves from seismic waves propagate upward.

d. **Postseismic signals:** Gravity waves from the seismic waves and the tsunami motion disturb the ionosphere with detectable amplitudes from satellites after calm of the main shock. On the other hand, the tsunami flow generates a magnetic field around it because of magnetohydrodynamic interaction.

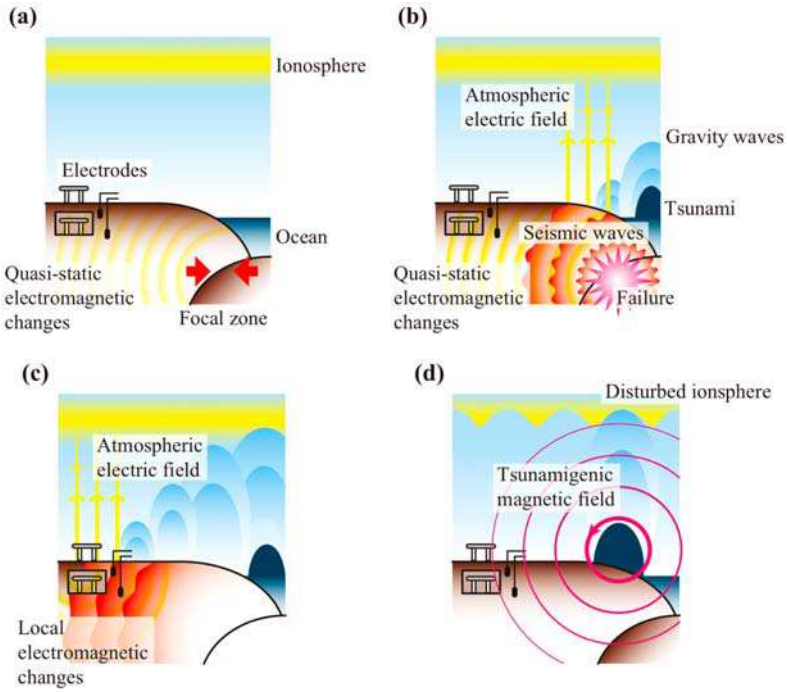

Fig. 19. Electric and electromagnetic phenomena classified in four stages before and after the occurrence of earthquakes: (a) Preseismic, (b) Co-faulting, (c) Coseismic, and (d) Postseismic

6. Appendix

The digital natural observation (D-NOB) method is a kind of linear transformation technique used to address the instantaneous nature of a signal waveform (Iijima, 2000, 2001). Linear transformation simplifies the quantitative evaluation of the output result. The outline of this method is the following:

First, an identical operator I and a delay operator D are defined respectively as

$$I f(n) = f(n) \text{ and} \tag{2}$$

$$D f(n) = f(n-1), \tag{3}$$

where $f(n)$ are arbitrary time series data. Using them, two operators are also defined as

$$\Gamma = (1-\lambda)I + \lambda D \text{ and} \tag{4}$$

$$\Lambda = \lambda I - \lambda D, \tag{5}$$

where λ ($0 < \lambda < 1$) is a weighting factor, normally 0.5. When an operator is assumed as

$$X_m^{(M)} = \Gamma^{M-m}\Lambda^m, \tag{6}$$

with m = 0, 1, 2, ..., M, the following equation is obtained.

$$n_m^{(M)}(n) = X_m^{(M)} f(n). \tag{7}$$

The $n_m^{(M)}(n)$ are time series data of the Mth degree and the mth order, called a fundamental observation value (FOV) corresponding to the time series data $f(n)$. They represent the instantaneous variation of the observed waveform at time n. From Eq. 7, the FOV is

$$n_m^{(M)} = \sum_{l=0}^{M} \binom{M}{l} (1-\lambda)^{M-l} \lambda^l \left\{ \left(\frac{\lambda}{1-\lambda} \right)^m k^{(M)}(m,l) \right\} f(n-l), \tag{8}$$

with m = 0, 1, 2, ..., M, where

$$k_m^{(M)}(m,l) = \frac{1}{\binom{M}{l}} \sum_{r=0}^{l} (-1)^r \binom{m}{r} \binom{M-m}{l-r} \left(\frac{1-\lambda}{\lambda} \right)^r, \tag{9}$$

with l = 0, 1, 2, ..., M and where $\binom{M}{m}$ represents the binomial coefficients.

Eq. (7) changes completely from $n_m^{(M)}(n)$ of the Mth order to the original data $f(n)$ using

$$f(n) = \sum_{m=0}^{M} \binom{M}{m} n_m^{(M)}(n). \tag{10}$$

Eq. (10) is called the NOB inverse transform. Eqs. (7) and (10) are collectively designated as the NOB-transform.

7. References

Balk, M., Bose, M., Ertem, G., Rogoff, D.A., Rothschild, L.J. & Freund, F.T. (2009). Oxidation of water to hydrogen peroxide at the rock-water interface due to stress-activated electric currents in rocks. *Earth and Planetary Science Letters*, Vol. 283, pp. 87–92.

Eftaxias, K., Frangos, P., Kapiris, P., Polygiannakis, J. Kopanas, J. & Peratzakis, A. (2004). Review and a model of pre-seismic electromagnetic emissions in terms of fractal electrodynamics. *Fractals*, Vol. 12, pp. 243–273.

Fraser-Smith, A.C., Bernardi, A. & McGill, P.R. (1990). Low-frequency magnetic field measurements near the epicenter of the Ms 7.1 Loma Prieta earthquake. *Geophysical Research Letters*, Vol. 17, pp. 1465–1668.

Galvan, D.A., Komjathy, A., Hickey, M.P. & Mannucci, A.J. (2011). The 2009 Samoa and 2010 Chile tsunamis as observed in the ionosphere using GPS total electron content. *Journal of Geophysical Research*, Vol. 116, pp. A06318.

Hayakawa, M., Kasahara, Y., Nakamura, T., Muto, F., Horie, T., Maekawa, S., Hobara, Y., Rozhnoi, A.A., Solovieva, M. & Molchanov, O.A. (2010). A statistical study on the correlation between lower ionospheric perturbation as seen by subionospheric VLF/LF propagation and earthquakes. *Journal of Geophysical Research*, Vol. 115, pp. A09305.

Iijima, T. (2000). *Theory of Natural Observation Method*, Morikita Publishing Company, Tokyo, pp. 194 (in Japanese).

Iijima, T. (2001). *The Digital Natural Observation Method*, Morikita Publishing Company, Tokyo, pp. 142 (in Japanese).

Kano, Y. & Yanagidani, T. (2006). Broadband hydroseismograms observed by closed borehole wells in the Kamioka mine, central Japan: Response of pore pressure to seismic waves from 0.05 to 2 Hz. *Journal of Geophysical Research*, Vol. 111, pp. B03410.

Liu, J.Y., Tsai, H.F., Lin, C.H., Kamogawa, M., Chen, Y.I., Lin, C.H., Huang, B.S., Yu, S.B. & Yeh, Y.H. (2010). Coseismic ionospheric disturbances triggered by the Chi-Chi earthquake. *Journal of Geophysics*, Vol. 115, pp. A08303.

Lockner, D.A., Johnston, M.D.S. & Byerlee, J.D. (1983). A mechanism to explain the generation of earthquake lights. *Nature*, Vol. 302, pp. 28–33.

McCarthy, D.F. (2006). *Essentials of Soil Mechanics and Foundations: Basic Geotechnics*, *7th Edition*, Prentice Hall, Upper Saddle River, pp. 864.

Muire-Wood R. & King, G.C.P., 1993. Hydrological signatures of earthquake strain. *Journal of Geophysical Research*, Vol. 98, pp. 22,035–22,068.

Okubo, K., Yamamoto, K., Takayama, M. & Takeuchi, N. (2005). Generation mechanism of Earth potential difference signal during seismic wave propagation and its observation condition. *IEEJ Transactions on Fundamental and Materials*, Vol. 125, pp. 614–618 (in Japanese with English abstract).

Okubo, K., Sato, S., Ishii, T. & Takeuchi, N. (2006a). Observation of atmospheric electricity variation signals during underground seismic wave propagation. *IEEJ Transactions on Electrical and Electronic Engineering*, Vol. 1, pp. 182–187.

Okubo, K., Yamamoto, K., Takayama, M. & Takeuchi, N. (2006b). Conditions of atmospheric electricity variation during seismic wave propagation. *Electrical Engineering in Japan*, Vol. 157, pp. 1–9.

Okubo, K., Takayama, M. & Takeuchi, N. (2007). Electrostatic field variation in the atmosphere induced by earthpotential difference variation during seismic wave propagation. *IEEE Transactions on Electromagnetic Compatibility*, Vol. 49, pp. 163–169.

Okubo, K., Takeuchi, N., Utsugi, M., Yumoto, K. & Sasai, Y. (2011). Direct magnetic signals from earthquake rupturing: Iwate-Miyagi earthquake of M7.2, Japan. *Earth and Planetary Science Letters*, Vol. 305, pp. 65–72.

Oyama, K., Kakinami, Y., Liu, J.Y., Kamogawa, M. & Kodama, T. (2008). Reduction of electron temperature in low-latitude ionosphere at 600 km before and after large earthquakes. *Journal of Geophysical Research*, Vol. 113, pp. A11317.

Pulinets, S.A., Boyarchuk, K.A., Hegai, V.V., Kim, V.P. & Lomonosov, A.M. (2000). Quasielectrostatic model of atmosphere-thermosphere-ionosphere coupling. *Advances in Space Research*, Vol. 26, pp. 1209–1218.

Rapoport, Y., Grimasky, V., Hayamawa, M., Ivchenko, Juarez-R, V.D., Koshevaya, S. & Gotynyan, O. (2004). Change of ionospheric plasma parameters under the influence of electric field which has lithospheric origin and due to radon emanation. *Physics and Chemistry of the Earth*, Vol. 29, pp. 579–587.

Rolland, L.M., Occhipinti, G., Lognonne, P. & Loevenbruk, A. (2010). Ionospheric gravity waves detected offshore Hawaii after tsunamis. *Geophysical Research Letters*, Vol. 37, pp. L17101.

Saradjian, M.R. & Akhoondzadeh, M. (2011). Thermal anomalies detection before strong earthquakes (M > 6.0) using interquartile, wavelet and Kalman filter methods. *Natural Hazards and Earth System Sciences*, Vol. 11, pp. 1099–1108.

Smith, G. N. (1982). *Elements of Soil Mechanics for Civil and Mining Engineers*, *5th Revised Edition*, Collins, London, pp. 512.

Takeuchi, A., Okubo, K., Watanabe, S., Nakamura, Y. & Takeuchi, N. (2009). Electric and Ionic Environmental Circumstances Interacting at Hosokura Underground Mine in Northeast Japan. *IEEJ Transactions on Fundamental and Materials*, Vol. 129, pp. 870–874.

Takeuchi, A., Futada, Y., Okubo, K. & Takeuchi, N. (2010). Positive electrification on the floor of an underground mine gallery at the arrival of seismic waves and similar electrification on the surface of partially stressed rocks in laboratory. *Terra Nova*, Vol. 22, pp. 203–207.

Takeuchi, N., Narita, K., Ono, I., Goto, Y. & Chubachi, N. (1995). Measurement of seismic wave with vertically induced Earth potential difference. *Transactions of IEE of Japan*, Vol. 115-C, pp. 1548–1553 (in Japanese with English abstract).

Takeuchi, N., Chubachi, N. & Narita, K. (1997a). Observation of earthquake waves by the vertical earth potential difference method. *Physics of the Earth and Planetary Interiors*, Vol. 101, pp. 157–161.

Takeuchi, N., Chubachi, N., Narita, N. Honma, N. & Takahashi, T. (1997b). Characteristics of vertical earth potential difference signals. *Transactions of IEE of Japan*, Vol. 117-C, pp. 554–560, (in Japanese with English abstract).

Takeuchi, N., Okubo, K. & Honma, N. (2000). Potential variations of metal electrode in the air during seismic wave propagation. *Transactions of IEE of Japan*, Vol. 120-C, pp. 1409–1415 (in Japanese with English abstract).

Tyler, R.H. (2005). A simple formula for estimating the magnetic field generated by tsunami flow. *Geophysical Research Letters*, Vol. 32, pp. L09608.

Uyeda, S., Nagao, T. & Kamogawa, M. (2009). Short-term earthquake prediction: Current status of seismo-electromagnetics. *Tectonophysics*, Vol. 470, pp. 205–213.

Varianatos, P. (2005). *The Physics of Seismo Electric Signals*, Terra Scientific Publishing Company, Tokyo, pp. 338.

Yan, R., Chen, Y., Gao, F. W. & Huang, F.Q. (2008). Calculating skempton constant of aquifer from volume strain and water level response to seismic waves at Changping seismic station. *Acta Seismologica Sinica*, Vol. 21, pp. 148–155.

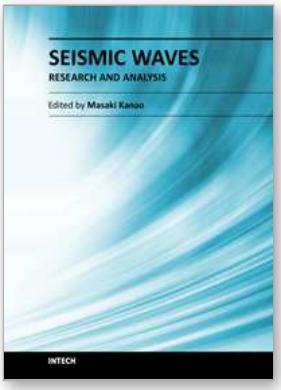

Seismic Waves - Research and Analysis

Edited by Dr. Masaki Kanao

ISBN 978-953-307-944-8
Hard cover, 326 pages
Publisher InTech
Published online 25, January, 2012
Published in print edition January, 2012

The importance of seismic wave research lies not only in our ability to understand and predict earthquakes and tsunamis, it also reveals information on the Earth's composition and features in much the same way as it led to the discovery of Mohorovicic's discontinuity. As our theoretical understanding of the physics behind seismic waves has grown, physical and numerical modeling have greatly advanced and now augment applied seismology for better prediction and engineering practices. This has led to some novel applications such as using artificially-induced shocks for exploration of the Earth's subsurface and seismic stimulation for increasing the productivity of oil wells. This book demonstrates the latest techniques and advances in seismic wave analysis from theoretical approach, data acquisition and interpretation, to analyses and numerical simulations, as well as research applications. A review process was conducted in cooperation with sincere support by Drs. Hiroshi Takenaka, Yoshio Murai, Jun Matsushima, and Genti Toyokuni.

InTech Europe
University Campus STeP Ri
Slavka Krautzeka 83/A
51000 Rijeka, Croatia
Phone: +385 (51) 770 447
Fax: +385 (51) 686 166
www.intechopen.com

InTech China
Unit 405, Office Block, Hotel Equatorial Shanghai
No.65, Yan An Road (West), Shanghai, 200040, China
中国上海市延安西路65号上海国际贵都大饭店办公楼405单元
Phone: +86-21-62489820
Fax: +86-21-62489821